Ceramics International 50 (2024) 50648–50656

Contents lists available at ScienceDirect

Ceramics International

journal homepage: www.elsevier.com/locate/ceramint

γ-radiation-induced centers in irradiated perovskite $SrCeO_3$ and their role in thermally stimulated reactions: Fluorescence, thermally stimulated luminescence, electron paramagnetic resonance and shielding studies

Vijay Singh [a,*], S. Watanabe [b], T.K. Gundu Rao [b], V.P. Singh [c], Nilo F. Cano [d]

[a] Department of Chemical Engineering, Konkuk University, Seoul, 05029, South Korea
[b] Institute of Physics, University of Sao Paulo, SP, 05508-090, Brazil
[c] Department of Physics, Karnatak University, Dharwad, India
[d] Instituto Do Mar, Universidade Federal de São Paulo, Rua Doutor Carvalho de Mendonça, 144, CEP 11070-100, Santos, SP, Brazil

ARTICLE INFO

Handling Editor: P. Vincenzini

Keywords:
Perovskite
$SrCeO_3$
γ-radiation
EPR
Defect centers
Thermoluminescence

ABSTRACT

One promising host for actinide radioactive wastes is orthorhombic perovskite-type oxide. Perovskite $SrCeO_3$ ceramic was synthesized by nitrate-fuel combustion, which includes the organic fuel glycine. Powder X-ray diffraction was utilized to determine the structural features, and γ-radiation-induced changes and shielding properties were investigated in perovskite $SrCeO_3$. In a mixed-phase sample, a bright sky-blue luminescence was observed, and two thermoluminescence (TL) peaks were seen in irradiated $SrCeO_3$ ceramic. Electron paramagnetic resonance (EPR) spectrum in γ-irradiated $SrCeO_3$ ceramic had contributions from five defect centers. Center I having an isotropic *g*-value equal to 2.0283, is ascribed to an O^- ion, while center II with an axial *g*-tensor with principal values $g_{||} = 2.0224$ and $g_{\perp} = 2.0068$ is determined as an O_2^- ion. O^- ion relates to the TL peak at 215 °C. Center III with a *g*-value equal to 2.0009 is identified as an F^+ center and is related to the 185 °C TL peak. The defect center associated with center IV is also identified as an F^+ center. An additional defect center in the higher field region of the spectrum is assigned to an F^+ center, and the center results from an F-center (oxygen vacancy with two electrons). The mass attenuation coefficients, effective atomic numbers, and half-value layer thicknesses concerning shielding property effectiveness were computed and it was found that the perovskite $SrCeO_3$ ceramic provided superior γ-shielding properties.

1. Introduction

Investigation of radiation-induced defects in solid materials and their roles under different applications has greatly improved over the last two decades [1–4]. Ionizing radiation is increasingly applicable in numerous research fields, including industry, medicine, and nuclear power production [5–8]. It is worth noting that the nuclear industry needs to find solutions for immobilizing radioactive waste for safe long-term storage. Borosilicate glass is used to immobilize these materials, and researchers have also investigated various categories of ceramic hosts and glass for many years [9–12]. The structure of perovskite-type ceramic hosts is significant for compacting a wide variety of radioactive waste elements to convert the crystalline forms of their constituent phases [13–16]. Findings in the literature suggest that the chemical and physical durability of radioactive waste-loading materials can contribute significantly to the successful isolation of nuclear waste [17–20]. Thus, the impacts of radiation on the chemical stability and physical characteristics of perovskite-type ceramic are of great importance.

The ABO_3 perovskite-type oxides have been investigated extensively, considering intriguing properties such as optical, superconductivity, ferroelectricity, and magnetism [21–24]. Perovskite oxide materials with large divalent A cations and tetravalent B cations are industrial functional compounds with several applications due to their magnetic, ion-exchange, ferroelectric, luminescent, catalytic, and semiconducting properties [25–30]. In recent years, cerium oxide-based perovskites have been studied owing to being widely used as catalytic and ceramic composite materials having fluorescence, high mechanical properties, and ion exchange [31–33]. The perovskite-oxide ceramics such as $SrCeO_3$ and $BaCeO_3$ have excellent proton conduction at elevated temperatures [34]. The structural stability of the $SrCeO_3$ ceramic is higher

* Corresponding author.
E-mail address: vijayjiin2006@yahoo.com (V. Singh).

https://doi.org/10.1016/j.ceramint.2024.09.409
Received 15 August 2024; Received in revised form 20 September 2024; Accepted 29 September 2024
Available online 30 September 2024

than that of the $BaCeO_3$ ceramic in a humid atmosphere [35]. In recent years, the physical properties of $SrCeO_3$ have been broadly investigated for characterizing fission product inclusions in immense burnup UO_2 nuclear fuel and potential applications in hydrogen-based fuel cells [36,37].

The B site of $SrCeO_3$ has moderate exchange by the trivalent rare earth (RE) cations to improve proton conductivity and chemical stability. $SrCeO_3$ doped with Yb^{3+}, Y^{3+}, or Sc^{3+} is known to produce a proton-conductive oxide in a hydrogen-containing atmosphere at elevated temperatures [38,39]. Yb^{3+}-doped $SrCeO_3$ perovskite materials are promising for H_2 separation membranes [40]. Liu et al. [41] studied the conductivity and the chemical stability of $SrCeO_3$ by substituting K^+ and Y^{3+} for Sr^{2+} and Ce^{4+}. They observed that substituting monovalent K^+ for divalent Sr^{2+} generated an adequately negative defect that charge-compensated due to the production of the sufficiently positive defect. Shandiz et al. [42] reported a low-temperature gas sensor via the fabrication of $SrCe_{0.9}Yb_{0.1}O_3$ as a proton conductor. Dong et al. [43] studied theoretical spin-Hamiltonian parameters in favor of the orthorhombic Pr^{4+} ion that occurs onto a $SrCeO_3$ crystal, and Sahu et al. [44] investigated solid-state speciation of uranium ions and their hot structure in Sr_2CeO_4 using time-resolved photoluminescence spectroscopy. In addition, they have explained the proper understanding of the photophysical properties of uranium ions with the help of the host Sr_2CeO_4 model host lattice.

Researchers have made considerable effort in the past few decades to design a novel luminescent system without RE doping because of the cost involved in RE mining and processing [45–47]. In this context, numerous studies have been performed on several luminescent systems without RE elements [48–51]. Cerium (Ce) is the most abundant, low-cost material among RE elements. Therefore, the alkaline earth cerium oxide luminescent system has been emerging as a significant area of research to replace traditional expensive RE luminescence systems [52,53]. Currently, there is a tremendous demand for focus on designing self-activated luminescent systems separate from defect-induced luminescence.

Though many studies are available on the synthesis and the luminescence properties of alkaline earth cerium oxide ceramics, the influence of defects in $SrCeO_3$ and their effects on luminescence has not been well investigated [54–56]. Therefore, we took a step forward using electron paramagnetic resonance (EPR) spectroscopy to understand the role and possible defects responsible for thermoluminescence (TL) in $SrCeO_3$. EPR is an effective technique for studying in-depth physical characteristics of paramagnetic defects in oxides, and EPR's radiation-induced defects have been extensively explored for its thermal, electrical, and optical studies [57–60]. Cerium is one of the promising candidates in the RE ions having 3+ and 4+ oxidation states which offers a suitable luminescence output under UV excitation. Concurrently, the optical properties and radiation-induced transformations have also been investigated for Ce ions in diverse aspects [61–63]. Many research papers have already been published on the luminescence studies of numerous cerium-doped systems, but as far as we found, none of the work has been reported on TL and EPR of gamma-irradiated $SrCeO_3$.

Generally, ceramic powder is synthesized by conventional solid-state reaction, which involves mixing powder reactants, such as oxides or carbonates, then calcining the mixture at a high temperature for a specific duration to obtain ceramic powders. Among various synthesis methods, combustion synthesis is a promising approach for obtaining ceramic with relatively low temperature and time. However, this method also has some issues of sensitivity that depend on the procedure of parameters. Thus, to achieve the optimum process, fuels recreate a substantial role in obtaining the pure phase of the sample by releasing sufficient heat during synthesis. In the present study, we characterized the $SrCeO_3$ ceramic prepared by varying amounts of glycine as a prevalent fuel. Next, we investigated the prepared products using X-ray diffraction (XRD) and photoluminescence (PL). We identified several defects formed by gamma irradiation in the sample and examined their roles in the TL glow peaks. In addition, we combined EPR and TL results to get the details regarding the identification and decomposition of defect centers in the $SrCeO_3$ system, and we investigated the shielding properties of $SrCeO_3$ ceramic using mass attenuation coefficients (μ/ρ), effective atomic numbers (Z_{eff}), and half-value layer (HVL) thickness.

2. Materials preparation, analysis, and computational method

2.1. Material preparation and analysis

We prepared the $SrCeO_3$ host by combusting $Sr(NO_3)_2$, $Ce(NO_3)_3{\cdot}6H_2O$, $C_2H_5NO_2$, and H_3BO_3 as precursor materials. We prepared the $SrCeO_3$ samples with two different compositions. In the first composition, we calculated the amount of precursor materials, keeping the oxidizer/fuel molar ratio = 1, the stoichiometric amount of 1.4812 g [$Sr(NO_3)_2$], 3.0394 g [$Ce(NO_3)_3{\cdot}6H_2O$], 1.4556 g ($C_2H_5NO_2$), and 0.047 g [H_3BO_3] materials were used as precursor materials, and this sample is here referred to as SC1. In the second composition, we used double the amount of fuel. We used the stoichiometric amounts of 1.4812 g [$Sr(NO_3)_2$], 3.0394 g [$Ce(NO_3)_3{\cdot}6H_2O$], 2.9112 g ($C_2H_5NO_2$) and 0.047 g [H_3BO_3] as precursor materials, and we refer to this sample as SC2. To complete the combustion, we placed all the precursor materials in a 150 ml glass beaker and mixed them into 20 ml of de-ionized water. The prepared solution was heated on a hot plate for 20 min to find a homogenous solution which was further transferred inside a preheated furnace with a temperature of 500 °C. After the reaction was completed, fluffy masses formed inside the glass beaker after being crushed by mortar and pestle to achieve a tenuous powder. In the next step, transferred achieved powders to an alumina crucible, followed by annealing in a furnace at 1000 °C for 2 h in an air medium. We then used the resulting powders for characterization. The detailed process of the synthesis is shown in the pictorial view in Fig. 1.

The crystal structure has been analyzed through powder XRD analysis with a Rigaku Miniflex-II diffractometer operated with the Bragg-Brentano focusing geometry, using CuKα radiation (λ = 1.5406 Å) for an X-ray source. XRD spectra were taken from the synthesized samples with a scanning rate of 5°/minute, and the 2θ range of 10 to 80°. The PL emission and excitation spectra were observed using a spectrofluorophotometer (RF-5301PC Shimadzu) fitted with a xenon lamp. In addition, we used a calibrated ^{60}Co gamma chamber to irradiate the sample with gamma rays. Thermo Scientific 4500 TL reader has been used for the TL measurements, and a Bruker EMX ESR spectrometer operated at X-band along 100 kHz modulation frequency for the EPR experiments. The g-factors of defect centers were determined by the diphenyl picryl hydrazyl used for a stock sample. In addition, we studied the EPR spectra operating a Bruker BVT 2000 variable temperature accessory with the function of temperature.

2.2. Computational method

Mass attenuation coefficients for gamma radiation of a compound material are computed by employing the mixture rule as follows,

$$\mu \Big/ \rho = \sum_i w_i (\mu/\rho)_i \tag{1}$$

where w_i is the fractional weight and $(\mu/\rho)_i$, is the total mass attenuation coefficient regarding the ith constituent in a compound. The μ/ρ value at the specific energy of an element can be calculated by Xcom software [64].

The half-value layer (HVL) is a suitable material parameter for gamma-ray interaction. It is used significantly at a certain thickness of the sample sheet, which is required to decrease the intensity of photon by 50 % from the initial value. In this instance, HVL described the effectiveness of gamma-ray shielding. HVL and mean free path (MFP)

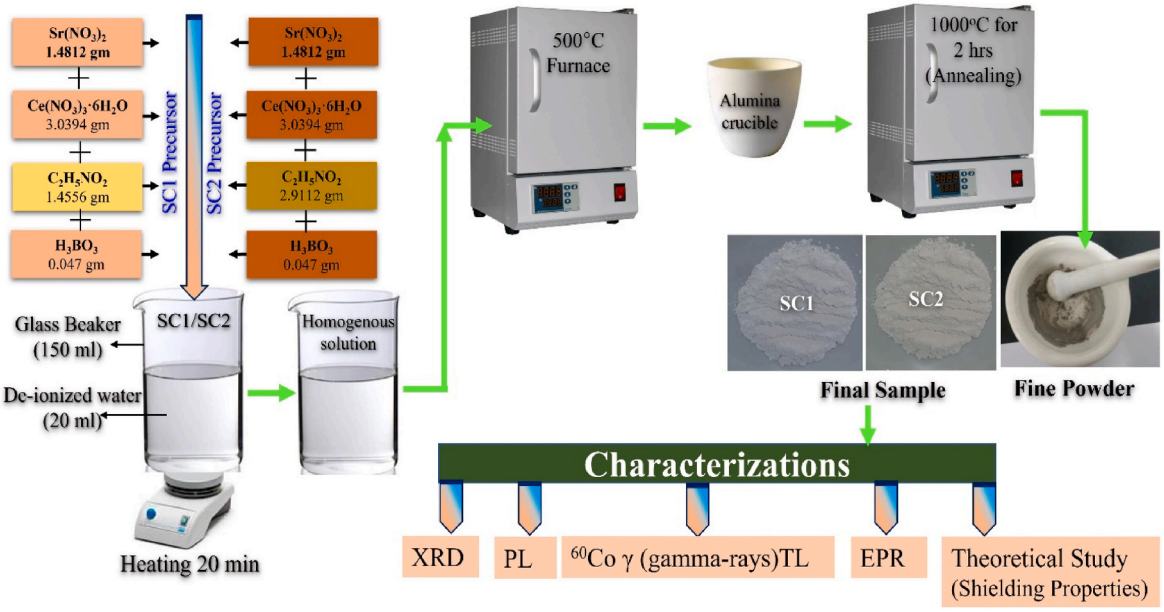

Fig. 1. Schematic representation of the synthesis of $SrCeO_3$ (SC1) and $SrCeO_3$ (SC2) ceramics.

were calculated applying the following equation:

$$HVL = \frac{0.693}{\mu} \tag{2}$$

where μ is the linear attenuation coefficient (cm^{-1}), and it is defined by the product of mass attenuation coefficient value (μ) and sample density (ρ).

Effective atomic number (Z_{eff}) is a fitting parameter concerning gamma-ray interactions and also comparable to the atomic number of elements, which explains compounds' properties concerning corresponding elements. Its properties also vary with energy. It can also be derived by the following equation [65].

$$Z_{eff} = \frac{\sigma_a}{\sigma_e} \tag{3}$$

where σ_a and σ_e are conductivity of atomic and electronic cross-sections respectively. It can be determined by applying the formula given below,

$$\sigma_a = \frac{\mu/\rho}{N_A \sum_i \frac{w_i}{A_i}} \tag{3a}$$

$$\sigma_e = \frac{1}{N_A} \sum_i \left(\sum_j \frac{f_j A_j}{A_j} \right) w_i \tag{3b}$$

3. Results and discussion

3.1. Crystal structure analysis

The XRD patterns of prepared $SrCeO_3$ (SC1) and $SrCeO_3$ (SC2) samples are displayed in Fig. 2. The XRD spectra for SC1 showed a dominant phase of the typical $SrCeO_3$ (JCPDS, 41–1689) and other peaks corresponding to Sr_2CeO_4 and CeO_2 phases. The pattern for SC2 indicated that the formation of the $SrCeO_3$ phase improved significantly but that there were few and very weak peaks of Sr_2CeO_4 and CeO_2 phases. In the XRD pattern for SC2, we observed that the amount of glycine rises preferred the structure of the $SrCeO_3$ phase; in SC2, the peak intensity of Sr_2CeO_4 and CeO_2 decreased significantly and most of them disappeared altogether. It implies that fuel plays a vital role in combustion synthesis. Zhang et al. [66] reported that in the SrO-CeO_2 system, at low temperature, the Sr_2CeO_4 is stable; however, as

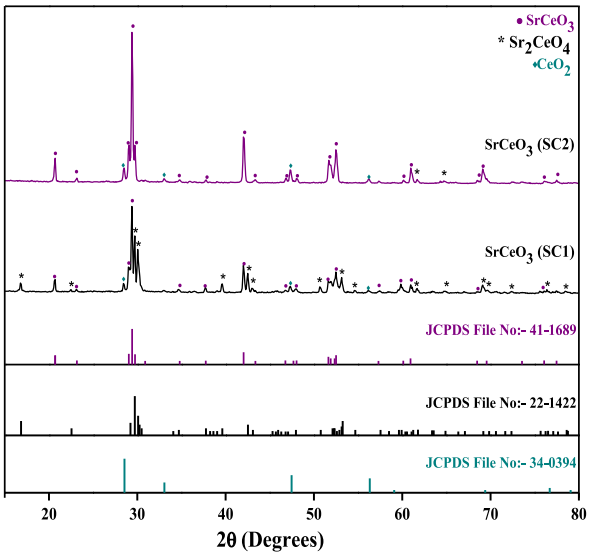

Fig. 2. Powder XRD patterns of $SrCeO_3$ (SC1) and $SrCeO_3$ (SC2) ceramics.

temperature increases, the $SrCeO_3$ phase becomes stable. Therefore, it can be concluded from the XRD results that the heat released during the combustion process after we increased the amount of glycine was sufficient to form an adequate crystalline $SrCeO_3$ phase. Fig. 3 shows the crystal structure of the $SrCeO_3$ host, it has an orthorhombic perovskite type with the *Pnma* space group. The $SrCeO_3$ crystal structure construct is based on Ce^{4+} octahedra states through distributing corners system; the Sr^{2+} ion occupies the center of the octahedra. Moreover, Sr and Ce ions have 8 and 6 coordination numbers, respectively.

3.2. Photoluminescence analysis

Fig. 4 shows PL spectra of $SrCeO_3$ (SC1) and $SrCeO_3$ (SC2) samples. Fig. 4 (a and b) represent the excitation and emission spectra (plotted by a red line) of SC1, respectively. The excitation spectrum exhibits an intense band over a maximum of 270 nm and a weak shoulder at 334 nm. It is noteworthy that cerium atoms persist in two oxidation states,

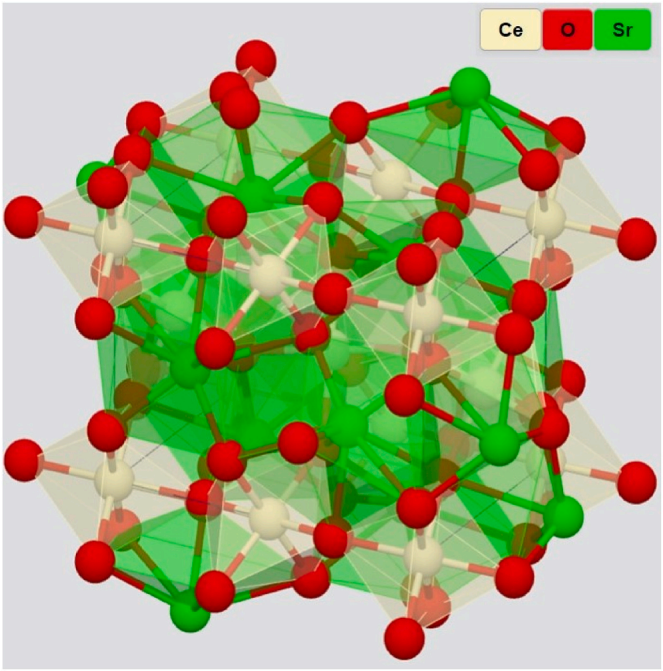

Fig. 3. General view of $SrCeO_3$ crystal structure.

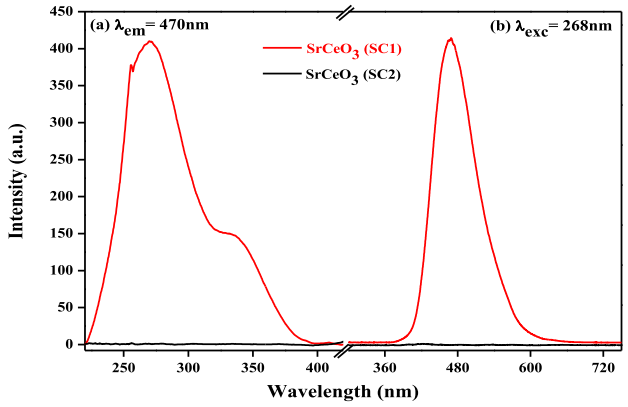

Fig. 4. Photoluminescence spectra of SC1 and SC2 ceramics (a) Excitation spectrum (λ_{em} = 470 nm) and (b) Emission spectrum (λ_{exc} = 270 nm).

either 3+, which is fully reduced, or 4+ fully oxidized states. Mostly the lanthanides are stable only in the trivalent structure, while cerium shows unique stability in the tetravalent structure. It has 4f and 5d partially filled subshells with the prediction of multiple excited substate. Seema and Nandakumar [67] reported two different bond lengths in Ce^{4+}-O^{2-} lattice structure; hence Sr_2CeO_4 phosphor exhibited a peak at 254 nm excitation, including a small hump near 267 nm. Furthermore, they conclude that these excitation peaks owe distinct charge transfer transitions [67]. Gupta et al. [68] studied the luminescence properties of Sr_2CeO_4 phosphor, and their excitation spectra represented dual peaks, a broad peak at 315 nm other a small hump at 360 nm. Moreover, Seo et al. [69] studied the excitation spectra of Sr_2CeO_4 and found a broadband peak at 299 nm and a small hump at 349 nm owing to the Ce^{4+} ions charge transfer states for t_{1g}-f and t_{1u}-f correspondingly. Grzyb et al. [70] studied Sr_2CeO_4 phosphor, and their excitation spectrum showed a wide asymmetric peak consisting of several peaks, 243, 296, and 330 nm. Earlier, Li et al. [71] demonstrated that the peak at 296 nm comes from the overlap of the dual residual peaks, and the peak at 243 nm is related to the O1→Ce^{4+} transition; O1 denoted terminal oxygen in Sr_2CeO_4; furthermore, 330 nm peak is due to the CT transition within the equatorial oxygen ion and Ce^{4+} ion (O2→Ce^{4+}) [71].

Fig. 4(b) represents the emission spectrum of SC1 under the excitation wavelength at 270 nm. A single broadband peak observed at 470 nm was attributed to the Ce^{4+} charge transfer emission. Seema and Nandakumar [67] reported a similar emission broadband peak at 470 nm for the Sr_2CeO_4 phosphor, although the excitation wavelength was 267 nm. A previous report stated that the 4f shell is empty in Ce^{4+}; hence the transition is possible because the oxygen ligand excites the electron upon the Ce^{4+} ion (CT transition of Ce^{4+}-O^{2-}) [68]. In addition, Seo et al. [69] reported that owing to the radiative relaxation process, a broad emission peak observed at 478 nm comes through the CeO_6 octahedra excited charge transfer state. Li et al. [71] observed that Sr_2CeO_4 exhibits a broadband peak at 475 nm, ascribed to the CT transition of Ce^{4+}-O^{2-}; Seema and Nandakumar [67] reported the broad emission band at 467 nm with Sr_2CeO_4.

For the luminescence of SC1, the excitation and emission spectra probably appeared because of the mixed phase of $SrCeO_3$ and Sr_2CeO_4. The differences between the excitation and emission spectra peak positions are noticeable because SC1 was not pure Sr_2CeO_4; it was a mixed phase of $SrCeO_3$ and Sr_2CeO_4. On the other hand, SC2 prepared under the same experimental conditions observed no excitation spectrum. From the XRD results of SC2 (Fig. 2), it was confirmed that there was no prominent XRD peak in the Sr_2CeO_4 phase, whereas SC1 consisted of several peaks because of Sr_2CeO_4. Therefore, the emission peak of SC1 (470 nm) can be attributed to O2p – Ce4f transition which corresponds to a band gap of 2.6 eV. This is in agreement with the calculated band gap of 2.2 eV for Sr_2CeO_4 using DFT method, as reported by Goubin et al. [72]. The band gap calculated through DFT is smaller than the experimental value. This discrepancy is due to the difficulty of properly describing localized orbitals in DFT calculations [72]. DFT often underestimates band gaps because it struggles to accurately describe the exchange-correlation energy, especially for materials with strongly localized d or f orbitals. Moreover, the presence of the shoulder peak and broadening of the PL peak is associated with the coupling between the electronic states and phonon energies. Sr_2CeO_4 exhibits several phonon modes associated with the vibrations of the CeO_6 octahedra and the Sr-O framework [73]. The Raman active modes typically appear in the range of 100–1000 cm^{-1} [74]. These phonon modes lead to a distribution of emission energies. Fig. 5 (a and b) represent the photographs of the $SrCeO_3$ (SC1) and $SrCeO_3$ (SC2) samples in daylight, and Fig. 5 (c and d) show the pictures of the $SrCeO_3$ (SC1) and $SrCeO_3$ (SC2) samples in UV light (254 nm), respectively. Similar to the PL results, $SrCeO_3$ (SC1) shows a strong sky-blue color under UV (254 nm) radiation, whereas $SrCeO_3$ (SC2) had no color. Next, estimated the Commission Internationale de l'Eclairage coordinates for $SrCeO_3$ (SC1) and plotted them in Fig. 6; again, $SrCeO_3$ (SC1) shows emission in the sky blue (0.1436, 0.2284) region. In the next section, we investigated TL and EPR on gamma irradiated SC2.

3.3. Thermoluminescence and radiation-induced defect centers

$SrCeO_3$ displays two thermoluminescence glow peaks at about 185 °C and 215 °C after γ-irradiation (dose: 10 Gy). The peak at 215 °C is prominent; the peak at 185 °C has relatively lower intensity. Glow curves were analyzed at a heating rate of 4 °C/s, and the observed glow curve is represented in Fig. 7.

Fig. 8 (a) presents the room temperature EPR spectrum of γ-irradiated $SrCeO_3$ material. Several defect centers contribute to the observed spectrum, and these are indicated in Fig. 8 (a). Center I is described by an individual line with a *g*-value of 2.0283 and a line width of 33 G. The spectrum recorded after annealing at 220 °C of the γ-irradiated sample is also presented in Fig. 8(b). Here, the lines from center II are more clearly seen with minimum overlap from adjoining EPR lines. Fig. 8(c) is the

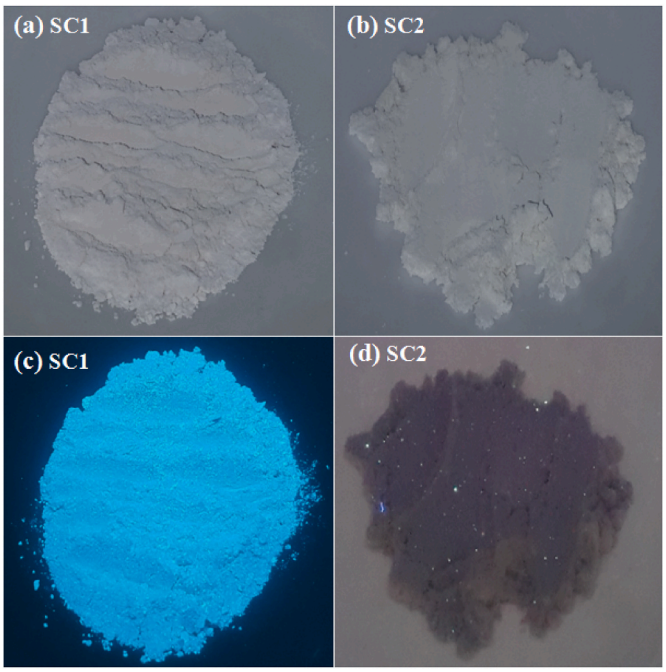

Fig. 5. Typical photographs of $SrCeO_3$ (SC1 and SC2) ceramics (a & b) sample under a room light and (c & d) under UV-254 nm.

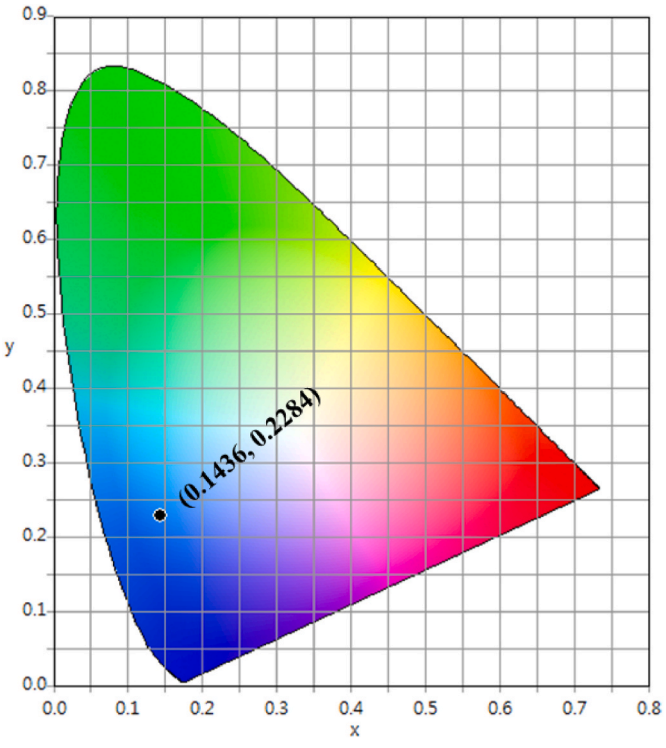

Fig. 6. Commission Internationale de l'Eclairage (CIE) diagram for $SrCeO_3$ (SC1) ceramic.

spectrum of the unirradiated $SrCeO_3$ phosphor. A single line is seen in the high field part of the spectrum, and this is labeled as A. This line most likely arises from an impurity ion.

$SrCeO_3$ is among the oxide compounds of ABO_3 perovskite in which large cations occupy A-sites and smaller cations are located at B-sites. $SrCeO_3$ crystallizes in the orthorhombic identical structure to $GdFeO_3$ [75]. CeO_6 octahedra are perfectly regular; the average bond length is

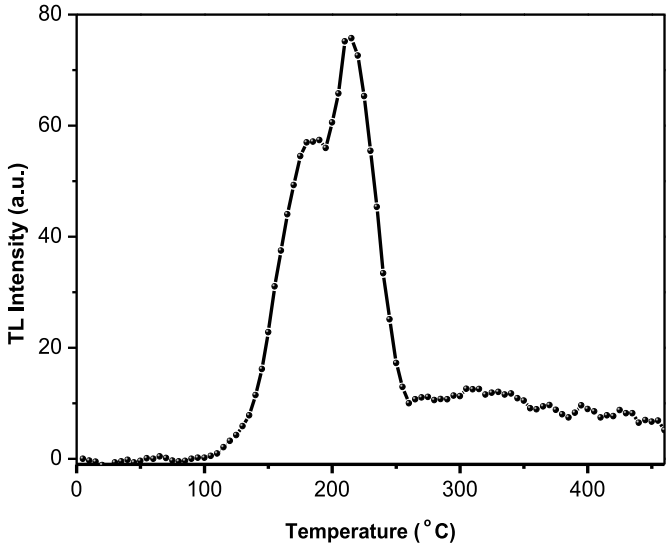

Fig. 7. Thermoluminescence glow curve of $SrCeO_3$ (Dose:10 Gy) showing thermoluminescence peaks at 185 °C and 215 °C.

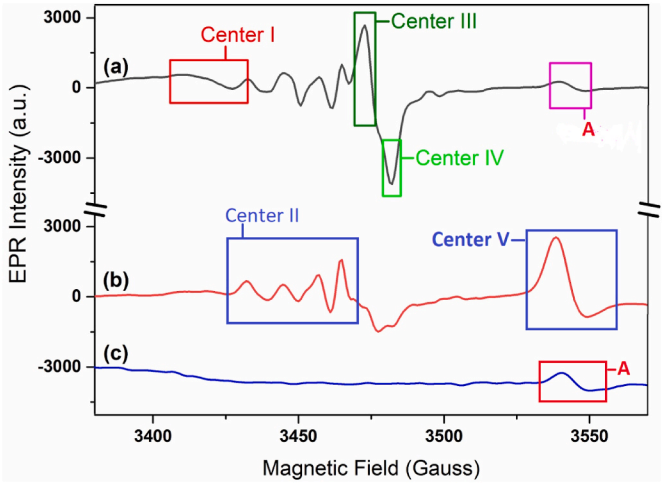

Fig. 8. (a) Room temperature EPR spectrum of irradiated $SrCeO_3$ ceramic (gamma dose: 10 kGy). The line labeled as I is due to an O^- ion. Centers III and IV are attributed to F^+ centers. (b) Spectrum recorded after thermal annealing at 220 °C. Lines labeled as center II are assigned to an O_2^- ion. Center V is attributed to an F^+ center. (c) EPR spectrum of the unirradiated $SrCeO_3$ ceramic. Line labeled as A is due to an unknown impurity ion.

2.246 Å and Ce^{3+} ions occupy octahedral sites with six-fold coordination provided by oxygen ions. On the other hand, Sr^{2+} ions are coordinated toward the triangular prism center, as observed in $GdFeO_3$.

Divalent Sr^{2+} ions and tetravalent Ce^{4+} are present in $SrCeO_3$ lattice. A partial replacement of Ce^{4+} ion by Sr^{2+} is possible due to antisite cation disorder and is shown as point defects in crystalline materials. Based on theoretical calculations, disorders are calculated to be present in crystals [76]. The experimental investigations have confirmed the presence of these defects [77,78]; moreover, such defects were identified using advanced microscopic techniques [79]. The cation disorder and non-stoichiometry in $SrCeO_3$ result in the generation of oxygen vacancies in the lattice. There is ease in the creation of oxygen vacancies in a lattice with cation exchange disorder [80].

Lattice defects form in oxides with cation disorder and non-stoichiometry, and these defects are the precursors of trapping centers [81]. For instance, after irradiation, electrons are able to get trapped in oxygen vacancies to create F^+ centers. O^- ions might be generated by

trapping holes at Sr and Ce vacancies [82]. Holes are localized on oxygen ions and the unpaired spin resides in an oxygen p orbital in O^- ion. Stability is given by the cation vacancies close to the O_2^-ion by way of electrostatic attraction. The model of an O^- ion with a hole trapped in a p_z -orbital on oxygen achieves a positive *g*-shift. The obtained *g*-value of center I indicates a positive *g*-shift, and the line is broad (line width ~ 33 G), which suggests a delocalization of the unpaired electron and connection to the nearby cations or impurities.

Consequently, center I is ascribed to an O^- ion, and the ion's stability results from a cation vacancy, i.e., Sr^{2+}/Ce^{4+} vacancy. X-irradiated $MgAl_2O_4$ spinel has been studied by Ibarra et al. [83]. The defect center observed in $MgAl_2O_4$ has similar characteristics as center I in the present study. Ibarra et al. have inferred based on optical absorption and ESR studies that the center results from hole trapping at oxygen ions surrounding cation vacancies [V-type center].

The thermal stability of center I was evaluated by applying the pulsed thermal annealing technique. The technique involves heating the sample to a specific temperature and then maintaining it for the next 3 min; after that, cooling it to room temperature for EPR measurements. The result of thermal annealing of center I is presented in Fig. 9. It shows that the center turns unstable at 180 °C and decays at a temperature between 180 °C and 250 °C. This decay of the defect center may correlate with the TL peak of 215 °C.

In contrast to other defect centers in the $SrCeO_3$ system, center II exhibits hyperfine interaction with a spin ½ nucleus. Each line corresponding to parallel and perpendicular components of the *g*-tensor is split into two lines. The ESR lines associated with center II can be described by an axially symmetric *g*-tensor with principal values $g_{\parallel} = 2.0224$ and $g_{\perp} = 2.0068$, and the corresponding hyperfine splitting are $A_{\parallel} = 12.6$ G and $A_{\perp} = 12.2$ G, respectively. γ-irradiation of oxide systems generally create F-centers, F^+ centers (anion vacancy that has trapped an electron), and V-centers [78].

Another likely center to be formed is the superoxide ion, O_2^-. The formation mechanism of O_2^- ion has been explained by EPR investigations that invoke a direct transfer of an electron from the oxide surface to an adsorbed oxygen molecule. An alternate path has also been considered that takes place with the help of anion intermediates [84].

Garrone et al. [84] have observed in their study of MgO that superoxide ion O_2^- displays an axial g-tensor with principal values $g_{\parallel} = 2.070$ and $g_{\perp} = 2.0080$. O_2^- ion has also been identified in several oxides and zeolites [85–87] and exhibits considerable *g*-anisotropy. Moreover, $g_{\parallel}$ value of O_2^- ion depends on the host system and can vary between 2.0150 and 2.0800. The crystal field produced by the neighbouring cations controls the magnitude of $g_{\parallel}$- value. Considering these results, center II in $SrCeO_3$ with a comparatively large anisotropy in g-value is ascribed to an O_2^- ion. Fig. 9 shows the thermal annealing results of center II. As there is overlap from the center I, center II intensity could not be appropriately measured up to 200 °C. It is noticed that center II is unstable around 270 °C and decays in the range 270 °C–330 °C. As the observed TL peaks in $SrCeO_3$ are at 185 °C and 215 °C, center II could not be associated with the TL peaks.

In oxide systems, a likely center that can form is the F^+ center. In the first observation of this center in an alkali halide, it displayed a large line width of approximately 100 G [88]. F^+ centers display *g*-values close to the free-electron value (2.0023). The intrinsic linewidth of the center is very small and is about 1 Gauss [89].

The amount of electron delocalization and consequently the spin density at the nearest neighbours determines the line width. Generally, in alkali halides, there is an interaction of the unpaired electron with neighbours and also with ions from successive shells resulting in large line widths. Such is the case in systems like KCl and LiCl which display line widths of 20 Gauss and 58 Gauss respectively [90].

Besides alkali halides, F^+ centers can also be seen in oxides. As a result of irradiation, an electron is trapped at an anion vacancy. F^+ centers display positive or negative g-shifts, and the *g*-value is observed to be close to the free-spin value (2.0023). Center III in the present study displays a *g*-value (g = 2.0009) close to the free-spin value. Considering the possible defect centers that can be formed in $SrCeO_3$ and the observed features, center III is assigned to an F^+ center. Due to the reasons mentioned earlier, oxygen vacancies are present in the lattice, and it is not difficult to envisage the formation of an F^+ center wherein an electron is trapped due to irradiation at an oxygen vacancy. The thermal annealing behavior of the center is displayed in Fig. 9. It can be seen that center III decays in the temperature range of 110 °C–220 °C. This decay is related to the observed TL peak at 185 °C.

The line labeled as Center IV in Fig. 8 is characterized by the *g*-value 2.0040 with a line width of 8 Gauss. Considering the reasons for the assignment of center III, Center IV is also identified as an F^+ center.

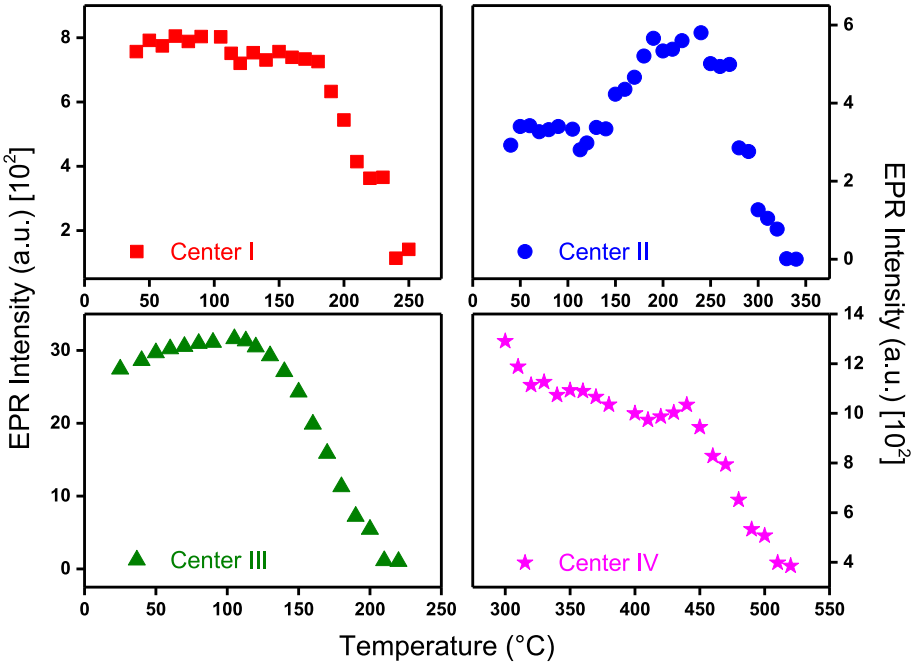

Fig. 9. Thermal annealing behavior of center I (O^- ion), center II (O_2^- ion), center III (F^+ center), and center IV (F^+ center) in $SrCeO_3$ ceramic.

Fig. 9 presents the thermal annealing behavior of the center. There is a considerable overlap of nearby lines with the ESR line of center IV and it was not possible to measure the intensity of the center till 300 °C. It is seen that the center starts decomposing around 440 °C and decays around 520 °C. It was not possible to associate the center with the observed TL peaks in the phosphor.

Fig. 10 shows the EPR spectrum after thermal annealing of the irradiated phosphor at 400 °C. Here, other centers have decayed, and lines from centers IV and V are seen. Center V shows an axially symmetric *g*-tensor with principal values $g_{\parallel} = 1.9464$ and $g_{\perp} = 1.9604$. The *g*-shifts are relatively small, and the line width is approximately 15 G. Center V is also assigned to an F^+ center. F^+ center normally exhibits an isotropic *g*-value, and center V displays an axially symmetric *g*-tensor. In some previous studies, for example in yttria-stabilized zirconia (ZrO_2:Y, YSZ) [91] as well as in $CaZrO_3$:Tb [92], a center that displays an axially symmetric *g*-tensor is observed. The *g*-values were found to be lower than the free-electron value in YSZ ($g_{\parallel} = 1.996$ and $g_{\perp} = 1.972$) and the centers in these systems were assigned to F^+ centers. The axial nature of the *g*-tensor in YSZ was ascribed to the existence of a symmetry-breaking defect at a nearby anionic site. A neutral F center (oxygen vacancy with two electrons) was considered as the symmetry-breaking defect. The neutral F-center can form due to the large density of oxygen vacancies in YSZ. Center V in $SrCeO_3$ is tentatively identified as an F^+ center and to explain the observed features, it needs to be located close to an F center. Due to the reasons stated previously, oxygen vacancies also appear in the $SrCeO_3$ lattice. Thus, F-center can form close to center V after irradiation.

The thermal annealing behavior of center V is shown in Fig. 11. The impurity ion EPR line (A) is seen till 100°C. At about 110 °C, center V line becomes visible at about the same position as the impurity ion and its intensity increases till about 190 °C. This kind of behavior has also been observed for the E_1'-center (an oxygen vacancy having an unpaired electron in a sp^3 hybrid orbital) in quartz. Jani et al. have explored in detail the formation and thermal annealing of E_1'-center [93]. This investigation enabled Jani et al. to propose that an oxygen vacancy with two electrons in a singlet state (S = 0) is the precursor of E_1'-center. It was suggested that the precursor releases an electron during post-irradiation annealing leading to the formation of E_1'-center. On the basis of these observations in SiO_2, it is suggested that the increase in the concentration of F^+ center (center V) in $SrCeO_3$ phosphor during the 100 °C–190 °C annealing region is due to the release of an electron from the precursor of F^+ center (i.e., F center). Oxygen vacancies present in $SrCeO_3$ lattice, due to non-stoichiometry and other reasons mentioned earlier, are converted into F centers (oxygen vacancies with two electrons) due to irradiation. During heating, these F centers release an electron leading to the growth of F^+ center (center V). The thermal annealing behavior shown in Fig. 11 is in accordance with this expectation.

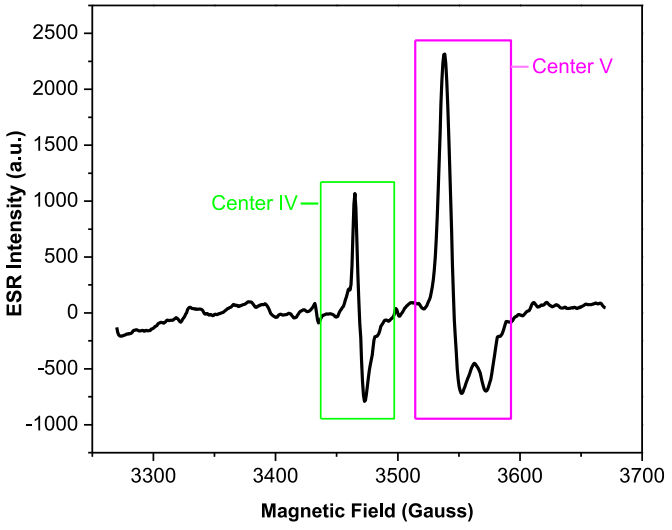

Fig. 10. EPR spectrum of irradiated $SrCeO_3$ ceramic after thermal anneal at 400 °C. Lines from centers IV and V are clearly seen.

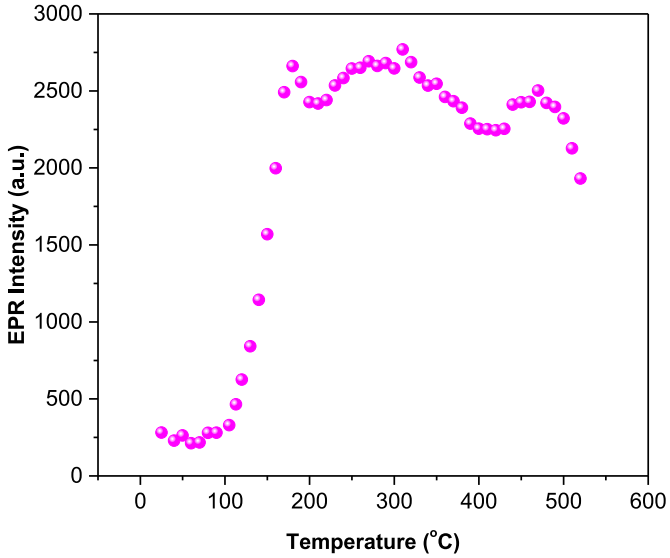

Fig. 11. Thermal annealing behavior of center V (F^+ center) in $SrCeO_3$ ceramic.

3.4. Shielding properties

Table 1 provides shielding parameters (μ/ρ, HVL, and Z_{eff}) of $SrCeO_3$ ceramic compared with ordinary concrete for photon energy 1 keV to 100 GeV. We found that the μ/ρ for both materials initially reduced to the lowest values and then increased. Z_{eff} showed random patterns for both materials, and its variation was insignificant in the high-energy region. However, HVL for both materials was also reduced to the lowest values and then increased to become constant (i.e., negligible variation). It is to be noted that the shielding parameters (μ/ρ, HVL and Z_{eff}) for $SrCeO_3$ ceramic were superior to those for ordinary concrete, and it required less thick shielding material than ordinary concrete. It was evident that the $SrCeO_3$ ceramic also needed less material and space to achieve the same level of protection against radiation. The differences in shielding parameters can be divided among three regions, low, medium, and high-energy photons, to explain the dependency of an atomic

Table 1
Shielding properties of $SrCeO_3$ ceramic and ordinary concrete.

Energy (MeV)	$SrCeO_3$			Ordinary Concrete		
	μ/ρ	HVL	Z_{eff}	μ/ρ	HVL	Z_{eff}
0.001	6683.90	1.84×10^{-5}	31.94	3348.00	9.00×10^{-5}	9.27
0.01	126.64	9.72×10^{-4}	51.15	22.93	1.31×10^{-2}	13.82
0.1	1.54	8.01×10^{-2}	48.30	0.17	1.74	10.34
1	0.06	2.07	24.94	0.06	4.73	9.91
10	0.04	3.44	32.30	0.02	1.32×10^{1}	10.25
100	0.06	2.09	38.96	0.02	1.31×10^{1}	10.84
1000	0.07	1.70	39.26	0.03	1.09×10^{1}	10.88
10000	0.08	1.63	39.24	0.03	1.05×10^{1}	10.89
100000	0.08	1.62	39.22	0.03	1.04×10^{1}	10.88

number of elements and photon energy for the photoelectric effect, Compton scattering, and pair production, respectively.

4. Conclusions

We investigated defects induced in perovskite $SrCeO_3$ by a ^{60}Co gamma source and shielding effectiveness against gamma radiation. We found that the amount of glycine played a vital role in the synthesizing orthorhombic perovskite $SrCeO_3$; specifically, increasing the amount of glycine completed combustion and brought results with better crystallinity. SC1 showed a bright sky-blue emission at 470 nm upon excitation at 270 nm. The luminescence from SC1 was most likely because of the presence of the Sr_2CeO_4 secondary phase. $SrCeO_3$ ceramic shows two TL peaks at 185 °C and 215 °C. Several defect centers have been identified in the irradiated $SrCeO_3$ phosphor and these are assigned to an O^- ion, O_2^- ion, and F^+ centers. It is observed that the O^- ion correlates with the 215 °C TL peak while the F^+ center (center III) correlates with the 185 °C TL peak. We also found that the $SrCeO_3$ ceramic was a superior shielding material to ordinary concrete with improved radiation protection.

CRediT authorship contribution statement

Vijay Singh: Writing – review & editing, Writing – original draft, Supervision, Investigation. **S. Watanabe:** Conceptualization. **T.K. Gundu Rao:** Formal analysis. **V.P. Singh:** Validation. **Nilo F. Cano:** Methodology.

Declaration of competing interest

The authors declare that they have no known competing financial interests or personal relationships that could have appeared to influence the work reported in this paper.

Acknowledgments

This work was supported by the National Research Foundation of Korea (NRF) grant funded by the Korea government (MSIT) (2018M2B2A9065656). This paper was supported by the KU Research Professor Program of Konkuk University.

References

[1] A. Hamedani, J. Byggmastar, F. Djurabekkova, G. Alahyarizadeh, R. Ghaderi, A. Minuchehr, K. Kai, Primary radiation damage in silicon from the viewpoint of a machine learning interatomic potential, Phys. Rev. Mater. 5 (2021) 114603.
[2] M.A. Tunes, M.M. Schneider, C.A. Taylor, T.A. Saleh, Rethinking radiation effects in materials science using the plasma-focused ion beam, J. Mater. Sci. 57 (2022) 16795–16808.
[3] A. Ozturk, M. Gencturk, K. Ahmed, Surface and size effects on the behaviors of point defects in irradiated crystalline solids, Front. Mater. 8 (2021) 684862.
[4] C. Dai, P. Saidi, B. Langelier, Q. Wang, C.D. Judge, M.R. Daymond, M. Mattucci, Radiation-induced segregation on dislocation loops in austenitic Fe-Cr-Ni alloys, Phys. Rev. Mater. 6 (2022) 053606.
[5] J.M. Cuttler, Application of low doses of ionizing radiation in medical therapies, Dose Response 18 (2020) 1559325819895739.
[6] A. Ashfaq, M.C. Clochard, X. Coqueret, C. Dispenza, M.S. Driscoll, P. Ulański, M. Al-Sheikhly, Polymerization reactions and modifications of polymers by ionizing radiation, Polymers 12 (2020) 2877.
[7] N. Manikanthababu, H. Sheoran, P. Siddham, R. Singh, Review of radiation-induced effects on β-Ga_2O_3 materials and devices, Crystals 12 (2022) 1009.
[8] D.M. Fleetwood, Radiation effects in a post-Moore world, IEEE Trans. Nucl. Sci. 68 (2021) 509–545.
[9] O.N. Koroleva, L.A. Nevolina, N.M. Korobatova, Glass-containing matrices based on borosilicate glasses for the immobilization of radioactive wastes, J. Comp. Sci. 7 (2023) 505.
[10] W. Wan, Y. Zhu, X. Zhang, D. Yang, Y. Huo, C. Xu, H. Yu, J. Zhao, J. Huo, B. Meng, Borosilicate glass-ceramics containing zirconolite and powellite for RE-and Mo-rich nuclear waste immobilization, Materials 14 (2021) 5747.
[11] X. Lu, L. Fan, X. Shu, S. Su, Y. Ding, F. Yi, Phase evolution and chemical durability of co-doped $Gd_2Zr_2O_7$ ceramics for nuclear waste forms, Ceram. Int. 41 (2015) 6344–6349.
[12] Z. Rák, R.C. Ewing, U. Becker, Role of iron in the incorporation of uranium in ferric garnet matrices, Phys. Rev. B 84 (2011), 155128-1-155128-10.
[13] S.K. Gupta, N. Pathak, R. Gupta, S.K. Thulasidas, V. Natarajan, Probing the oxidation state and coordination geometry of uranium ion in $SrZrO_3$ perovskite, J. Mol. Struct. 1068 (2014) 204–209.
[14] G. García-Rosales, R. Drot, F. Mercier-Bion, G. Lagarde, E. Simoni, Interaction between U(VI) and $SrTiO_3$ surfaces versus temperature, J. Colloid Interface Sci. 333 (2009) 104–113.
[15] H.B. Ortiz-Oliveros, E. Ordoñez-Regil, S.M. Fernández-Valverde, Sorption of uranium (VI) onto strontium titanate in KNO_3 medium, J. Radioanal. Nucl. Chem. 279 (2009) 601–610.
[16] C. Sabathier, J. Chaumont, J.-C. Krupa, Dose rate and temperature effects in radiation disorder creation in $SrTiO_3$, Nucl. Instrum. Methods Phys. Res. Sect. B Beam Interact. Mater. Atoms 196 (2002) 308–314.
[17] C.P. Kaushik, R.K. Mishra, P. Sengupta, A. Kumar, D. Das, G.B. Kale, K. Raj, Barium borosilicate glass - a potential matrix for immobilization of sulfate bearing high-level radioactive liquid waste, J. Nucl. Mater. 358 (2006) 129–138.
[18] R.C. Ewing, W.J. Weber, J. Lian, Nuclear waste disposal-pyrochlore ($A_2B_2O_7$): nuclear waste form for the immobilization of plutonium and "minor" actinides, J. Appl. Phys. 95 (2004) 5949–5971.
[19] J. Lian, K.B. Helean, B.J. Kennedy, L.M. Wang, A. Navrotsky, R.C. Ewing, Effect of structure and thermodynamic stability on the response of lanthanide stannate pyrochlores to ion beam irradiation, J. Phys. Chem. B 110 (2006) 2343–2350.
[20] J. Zhang, J. Lian, F. Zhang, J. Wang, A.F. Fuentes, R.C. Ewing, Intrinsic structural disorder and radiation response of nanocrystalline $Gd_2(Ti_{0.65}Zr_{0.35})_2O_7$ pyrochlore, J. Phys. Chem. C 114 (2010) 11810–11815.
[21] H. Gao, H. Yang, S. Wang, X.X. Zhao, Optical and electrochemical properties of perovskite type $MAlO_3$ (M=Y, La, Ce) pigments synthesized by a gamma-ray irradiation assisted polyacrylamide gel route, Ceram. Int. 44 (2018) 14754–14766.
[22] Y. Zhang, Y.L. Chen, C.H. Cheng, Y.J. Cui, Y. Zhao, Metal–insulator transition and superconductivity in Hg-doped $BaPb_{0.75}Bi_{0.25}O_3$, J. Phys. Chem. Solids. 72 (2011) 597–600.
[23] V. Yu Topolov, Effect of a tetragonal phase on heterophase states in perovskite-type ferroelectric solid solutions, Solid State Commun. 170 (2013) 1–5.
[24] R.A.P. Ribeiro, J. Andrés, E. Longo, S.R. Lazaro, Magnetism and multiferroic properties at $MnTiO_3$ surfaces: a DFT study, Appl. Surf. Sci. 452 (2018) 463–472.
[25] Y. Xue, J. Zhao, Y. Shan, H. Xu, Tunable magnetism in the $LaAlO_3/SrTiO_3$ heterostructure: Insights from first-principles calculations, Physica E 98 (2018) 120–124.
[26] Y. Inaguma, W. Mashiko, M. Watanabe, Y. Atsumi, N. Okuyama, T. Ohba, M/Li^+($M=Mg^{2+}$, Zn^{2+}, and Mn^{2+}) ion-exchange on lithium ion-conducting perovskite-type oxides and their properties, Solid State Ion 177 (2006) 2705–2709.
[27] X. Wu, Z. Wan, J. Qi, M. Wang, Ferroelectric photovoltaic properties of perovskite $Na_{0.5}Bi_{0.5}FeO_3$-based solution-processed solar cells, J. Alloys Compd. 750 (2018) 959–964.
[28] N. Singh, S. Kaur, M. Jayasimhadri, M.S. Pathak, S. Watanabe, T.K. Gundu Rao, J. K. Lee, V. Singh, UV emitting Pb^{2+} doped $SrZrO_3$ phosphors prepared by sol-gel procedure, Ceram. Int. 44 (2018) 17074–17078.
[29] G. Valderrama, A. Kiennemann, C.U. de Navarro, M.R. Goldwasser, $LaNi_{1-x}Mn_xO_3$ perovskite-type oxides as catalysts precursors for dry reforming of methane, Appl. Catal. A 565 (2018) 26–33.
[30] M. Mori, Y. Itagaki, Y. Sadaoka, Effect of VOC on ozone detection using semiconducting sensor with $SmFe_{1-x}Co_xO_3$ perovskite-type oxides, Sens. Actuator B Chem. 163 (2012) 44–50.
[31] X. Qi, Y.S. Lin, Electrical conduction and hydrogen permeation through mixed proton-electron conducting strontium cerate membranes, Solid State Ion 130 (2000) 149–156.
[32] T. Hibino, K. Mizutani, T. Yajima, H. Iwahara, Evaluation of proton conductivity in $SrCeO_3$, $BaCeO_3$, $CaZrO_3$ and $SrZrO_3$ by temperature programmed desorption method, Solid State Ion 57 (1992) 303–306.
[33] S. Yamanaka, K. Kurosaki, T. Matsuda, S.-I. Kobayashi, Thermal properties of $SrCeO_3$, J. Alloys Compd. 352 (2003) 52–56.
[34] Y.-P. Fu, C.-S. Weng, Effect of rare-earth ions doped in $BaCeO_3$ on chemical stability, mechanical properties, and conductivity properties, Ceram. Int. 40 B (2014) 10793–10802.
[35] S. Gopalan, A.V. Virkar, Thermodynamic stabilities of $SrCeO_3$ and $BaCeO_3$ using a molten salt method and galvanic cells, J. Electrochem. Soc. 140 (1993) 1060–1065.
[36] S. Yamanaka K. Kurosaki, T. Oyama, H. Muta, M. Uno, T. Matsuda, S.-I. Kobayashi, Thermophysical properties of perovskite-type strontium cerate and zirconate, J. Am. Ceram. Soc. 88 (2005) 1496–1499.
[37] G.C. Mather, D. Poulidi, A. Thursfield, M. Jesús Pascual, J.R. Jurado, I.S. Metcalfe, Hydrogen-permeation characteristics of a $SrCeO_3$-based ceramic separation membrane: thermal, ageing and surface-modification effects, Solid State Ion 181 (2010) 230–235.
[38] S. Yamanaka, M. Okada, S. Komatuki, M. Miyake, Hydrogen dissolution into Yb-doped $SrCeO_3$, J. Alloys Compd. 231 (1995) 713–715.
[39] H. Uchida, N. Maeda, H. Iwahara, Relation between proton and hole conduction in $SrCeO_3$-based solid electrolytes under water-containing atmospheres at high temperatures, Solid State Ion 11 (1983) 117–124.
[40] S. Yamanaka, M. Katsura, Desorption behavior of hydrogen and water from Yb-doped $SrCeO_3$, J. Alloys Compd. 275–277 (1998) 730–732.
[41] C. Liu, J.-J. Huang, Y.-P. Fu, C. Li, J.-Y. Wang, S. Lee, Effect of potassium substituted for A-site of $SrCe_{0.95}Y_{0.05}O_3$ on microstructure, conductivity and chemical stability, Ceram. Int. 41 (2015) 2948–2954.
[42] R.H. Shandiz, M. Shaterian, K. Ozaee, M. Enhessari, Fabrication of low temperature gas sensor using $SrCe_{0.9}Yb_{0.1}O_3$ nanopowders as proton conductor, Synth. React. Inorganic Met.-Org. Chem. 45 (2015) 1108–1111.

[43] H.-N. Dong, S.-Y. Wu, J. Liu, D.J. Keeble, Theoretical studies of the Spin Hamiltonian Parameters for the orthorhombic Pr^{4+} ion in $SrCeO_3$ crystal, J. Alloys Compd. 451 (2008) 705–707.

[44] M. Sahu, S.K. Gupta, D. Jain, M.K. Saxena, R.M. Kadam, Solid state speciation of uranium and its local structure in Sr_2CeO_4 using photoluminescence spectroscopy, Spectroc. Acta Pt. A-Molec. Biomolec. Spectr. 195 (2018) 113–119.

[45] X. Chen, Z. Xia, M. Yi, X. Wu, H. Xin, Rare-earth free self-activated and rare-earth activated $Ca_2NaZn_2V_3O_{12}$ vanadate phosphors and their color-tunable luminescence properties, J. Phys. Chem. Solids. 74 (2013) 1439–1443.

[46] J. Zhou, F. Huang, J. Xu, H. Chen, Y. Wang, Luminescence study of a self-activated and rare earth activated $Sr_3La(VO_4)_3$ phosphor potentially applicable in W-LEDs, J. Mater. Chem. C 3 (2015) 3023–3028.

[47] D. Song, C. Guo, T. Li, Luminescence of the self-activated vanadate phosphors $Na_2LnMg_2V_3O_{12}$ (Ln= Y, Gd), Ceram. Int. 41 (2015) 6518–6524.

[48] P. Feng, J. Zhang, C. Wu, X. Liu, Y. Wang, Self-activated afterglow luminescence of un-doped $Ca_2ZrSi_4O_{12}$ material and explorations of new afterglow phosphors in a rare earth element-doped $Ca_2ZrSi_4O_{12}$ system, Mater. Chem. Phys. 141 (2013) 495–501.

[49] T.-M. Chen, Y.-W. Chen, Systematic tuning of the luminescent properties of self-activated $ZnGa_2O_4$ phosphors by Cd ion substitution, J. Solid State Chem. 150 (2000) 204–208.

[50] S.-P. Kuang, Y. Meng, J. Liu, Z.-C. Wu, L.-S. Zhao, A new self-activated yellow-emitting phosphor $Zn_2V_2O_7$ for white LED, Optik 124 (2013) 5517–5519.

[51] T. Nakajima, M. Isobe, T. Tsuchiya, Y. Ueda, T. Manabe, Photoluminescence property of vanadates $M_2V_2O_7$ (M: Ba, Sr and Ca), Opt. Mater. 32 (2010) 1618–1621.

[52] Y. Tang, H. Guo Q. Qin, Photoluminescence of Sr_2CeO_4 phosphors prepared by microwave calcination and pulsed laser deposition, Solid Sate Commun 121 (2002) 351–356.

[53] J. Zhang, Z. Zhang, Z. Tang, Y. Lin, Mn^{2+} luminescence in (Ce, Tb)$MgAl_{11}O_{19}$ phosphor, Mater. Chem. Phys. 72 (2001) 81–84.

[54] X. Yu, X.H. He, S.P. Yang, X. Yang, X. Xu, Synthesis and luminescence of Sr_2CeO_4 superfine particles by citrate-gel method, Mater. Lett. 58 (2004) 48–50.

[55] S. Maensiri, C. Masingboon, P. Laokul, W. Jareonboon, V. Promarak, P. L. Anderson, Egg white synthesis and photoluminescence of platelike clusters of CeO_2 nanoparticles, Cryst. Growth Des. 7 (2007) 950–955.

[56] C.H. Park, C.H. Kim, C.H. Pyun, J.H. Choy, Luminescence of Sr_2CeO_4, J. Lumin. 87–89 (2000) 1062–1064.

[57] B. Boizot, G. Petite, D. Ghaleb, G. Calas, Radiation induced paramagnetic centers in nuclear glasses by EPR spectroscopy, Nucl. Instrum. Methods Phys. Res. Sect. B Beam Interact. Mater. Atoms 141 (1998) 580–584.

[58] M.A. Laruhin, H.J. van Es, G.R. Bulka, A.A. Turkin, D.I. Vainshtein, H.W. den Hartog, EPR study of radiation-induced defects in the thermoluminescence dating medium zircon ($ZrSiO_4$), J. Phys.-Condes. Matter 14 (2002) 3813–3831.

[59] R.M. Kadam, T.K. Seshagiri, V. Natarajan, S.V. Godbole, Radiation induced defects in $BaBPO_5$:Ce and their role in thermally stimulated luminescence reactions: EPR and TSL investigations, Nucl. Instrum. Methods Phys. Res. Sect. B Beam Interact. Mater. Atoms 266 (2008) 5137–5143.

[60] N. Veeraiah, Y. Gandhi, R.M. Kadam, B.J.R. Swamy, B. Suresh, V. Natarajan, V. R. Kumar, Study of gamma ray induced defect centers in MnO doped calcium fluoro borophosphate glasses by means of EPR spectroscopy, Mater. Lett. 167 (2016) 284–287.

[61] M. Kumar, M. Mohapatra, V. Natarajan, Luminescence characteristics of blue emitting $ZnAl_2O_4$: Ce nanophosphors, J. Lumin. 149 (2014) 118–124.

[62] B. Dhabekar, E.A. Raja, S. Menon, T.K.G. Rao, R.K. Kher, B.C. Bhatt, Identification of defect centers using TSL, PL, OSL and ESR studies in $LiAlO_2$ based phosphors, J. Phys D: App. Phys. 41 (2008) 115414.

[63] V. Singh, S. Watanabe, T.K.G. Rao, R.S. Kumaran, H. Gao, J. Li, H.-Y. Kwak, Characterization, luminescence, and defect centers of a Ce^{3+}-doped $Li_2Si_2O_5$ phosphor prepared by a solution combustion reaction, J. Electron. Mater. 44 (2015) 2736–2744.

[64] M.J. Berger, J.H. Hubbell, S.M. Seltzer, J. Chang, J.S. Coursey, R. Sukumar, D. S. Zucker, K. Olsen, XCOM: Photon Cross Section Database, National Institute of Standards and Technology, Gaithersburg, MD, 2010 (version 1.5). [Online] Available: http://physics.nist.gov/xcom. (Accessed 25 January 2018).

[65] V.P. Singh, N.M. Badiger, Gamma radiation interaction properties of space shielding materials, Journal of nuclear research and development 12 (2016) 41–44.

[66] C. Zhang, S. Li, X. Liu, X. Zhao, D. He, H. Qiu, Q. Yu, S. Wang, L. Jiang, Low temperature synthesis of Yb doped $SrCeO_3$ powders by gel combustion process, Int. J. Hydrog, Energy 38 (2013) 12921–12936.

[67] R. Seema, K. Nandakumar, A new synthetic pathway of Sr_2CeO_4 phosphor and its characterization, J. Lumin. 131 (2011) 2181–2184.

[68] S.K. Gupta, M. Sahu, K. Krishnan, M.K. Saxena, V. Natarajan, S.V. Godbole, Bluish white emitting Sr_2CeO_4 and red emitting Sr_2CeO_4:Eu^{3+} nanoparticles: optimization of synthesis parameters, characterization, energy transfer and photoluminescence, J. Mater. Chem. C 1 (2013) 7054–7063.

[69] Y.W. Seo, H.M. Noh, B.K. Moon, J.H. Jeong, H.K. Yang, J.H. Kim, Structural and luminescent properties of blue-emitting Sr_2CeO_4 phosphors by high-energy ball milling method, Ceram. Int. 41 (2015) 1249–1254.

[70] T. Grzyb, A. Szczeszak, J. Rozowska, J. Legendziewicz, S. Lis, Tunable luminescence of Sr_2CeO_4:M^{2+} (M = Ca, Mg, Ba, Zn) and Sr_2CeO_4:Ln^{3+} (Ln = Eu, Dy, Tm) nanophosphors, J. Phys. Chem. C 116 (2012) 3219–3226.

[71] L. Li, S. Zhou, S. Zhang, Investigation on charge transfer bands of Ce^{4+} in Sr_2CeO_4 blue phosphor, Chem. Phys. Lett. 453 (2008) 283–289.

[72] F. Goubin, X. Rocquefelte, M.H. Whangbo, Y. Montardi, R. Brec, S. Jobic, Experimental and theoretical characterization of the optical properties of CeO_2, $SrCeO_3$, and Sr_2CeO_4 containing Ce^{4+} (f^0) ions, Chem. Mater. 16 (2004) 662–669.

[73] D. Yadav, U. Kumar, S. Upadhyay, Study of structural, electrical, and photoluminescent properties of $SrCeO_3$ and Sr_2CeO_4, J. Adv. Ceram. 8 (2019) 377–388.

[74] Z. Chunxiang, S. Jianshe, Y. Xujie, L. Lude, W. Xin, Preparation, characterization and luminescence of Sm^{3+} or Eu^{3+} doped Sr_2CeO_4 by a modified sol-gel method, J. Rare Earths 28 (2010) 513–518.

[75] K.S. Knight, N. Bonanos, The crystal structures of some doped and undoped alkaline earth cerate perovskites, Mater. Res. Bull. 30 (1995) 347–356.

[76] M.M. Kuklja, Defects in yttrium aluminium perovskite and garnet crystals: atomistic study, J. Phys. Condens. Matter 12 (2000) 2953–2967.

[77] A.P. Patel, M.R. Levy, R.W. Grimes, R.M. Gaume, R.S. Frigelson, K.J. McClellan, C. R. Stanek, Mechanisms of nonstoichiometry in $Y_3Al_5O_{12}$, Appl. Phys. Lett. 93 (2008), 191902-191902-3.

[78] J. Dong, K. Lu, Noncubic symmetry in garnet structures studied using extended x-ray-absorption fine-structure spectra, Phys. Rev. B 43 (1991) 8808–8821.

[79] D. Truong, M.K. Devaraju, T. Tomai, I. Honma, Direct observation of antisite defects in $LiCoPO_4$ cathode materials by Annular dark- and bright-field electron microscopy, ACS Appl. Mater. Interfaces 5 (2013) 9926–9932.

[80] N. Yuan, X. Liu, F. Meng, D. Zhou, J. Meng, First-principles study of La_2CoMnO_6: a promising cathode material for intermediate-temperature solid oxide fuel cells due to intrinsic Co-Mn cation disorder, Ionics 21 (2015) 1675–1681.

[81] V. Singh, V. Kumar Rai, S. Watanabe, T.K. Gundu Rao, L. Badie, I. Ladoux-Rak, Y.-D. Jho, Synthesis, characterization, optical absorption, luminescence and defect centers in Er^{3+} and Yb^{3+} co-doped $MgAl_2O_4$ phosphors, Appl. Phys. 108 (2012) 437.

[82] M.S. Holston, J.W. McClory, N.C. Giles, L.E. Halliburton, Radiation-induced defects in $LiAlO_2$ crystals: holes trapped by lithium vacancies and their role in thermoluminescence, J. Lumin. 160 (2015) 43–49.

[83] A. Ibarra, F.J. Lopez, Jimenez de Castro, *V* Centers in $MgAl_2O_4$ Spinels B44, Phys. Rev., 1991, pp. 7256–7762.

[84] E. Garrone, A. Zecchina, F.S. Stone, Anionic intermediates in surface processes leading to O_2^-, formation on magnesium oxide, J. Catal. 62 (1980) 396–400.

[85] D.D. Eley, M.A. Zammitt, Spin centers and catalysis on γ-alumina, J. Catal. 21 (1971) 366–376.

[86] K.M. Wong, J.H. Lunsford, Electron paramagnetic resonance study of Y-type zeolites. III. O2- on AlHY, ScY, and LaY zeolites, J. Phys. Chem. 74 (1971) 1165–1168.

[87] J.H. Lunsford, ESR of adsorbed oxygen species, Catal. Rev. 8 (1973) 135–157.

[88] C.A. Hutchison, Paramagnetic resonance absorption in crystals colored by irradiation, Phys. Rev. 75 (1949) 1769–1770.

[89] J.E. Wertz, P. Auzins, R.A. Weeks, R.H. Silsbee, Electron spin resonance of F centers in magnesium oxide; confirmation of the spin of magnesium-25, Phys. Rev. 107 (1957) 1535–1537.

[90] W.C. Holton, H. Blum, Paramagnetic resonance of F centers in alkali halides, Phys. Rev. 125 (1962) 89–103.

[91] J.M. Costantini, F. Beuneu, D. Gourier, C. Trautmann, G. Calas, M. Toulemonde, Colour center production in yttria-stabilized zirconia by swift charged particle irradiations, J. Phys. Condens. Matter 16 (2004) 3957–3971.

[92] V. Singh, S. Watanabe, T.K. Gundu Rao, K. Al-Shamery, M. Haase, Y.D. Jho, Synthesis, characterisation, luminescence and defect centers in solution combustion synthesised $CaZrO_3$:Tb^{3+} phosphor, J. Lumin. 132 (2012) 2036–2042.

[93] M.G. Jani, R.B. Bossoli, L.E. Halliburton, Further characterization of the E1'center in crystalline SiO_2, Phys. Rev. B 27 (1983) 2285–2293.